Available online at www.sciencedirect.com
ScienceDirect
Journal of Power Sources 172 (2007) 296–307
JOURNAL OF POWER SOURCES
www.elsevier.com/locate/jpowsour

Performance analysis of a SOFC under direct internal reforming conditions

Vinod M. Janardhanan [a], Vincent Heuveline [b], Olaf Deutschmann [a,*]

[a] *Institute for Chemical Technology and Polymer Chemistry, Engesserstr 20, D-76131 Karlsruhe, University of Karlsruhe, Germany*
[b] *Institute for Applied and Numerical Mathematics, Kaiserstr. 12, D-76128 Karlsruhe, Germany*

Received 24 October 2006; received in revised form 8 June 2007; accepted 2 July 2007
Available online 12 July 2007

Abstract

This paper presents the performance analysis of a planar solid-oxide fuel cell (SOFC) under direct internal reforming conditions. A detailed solid-oxide fuel cell model is used to study the influences of various operating parameters on cell performance. Significant differences in efficiency and power density are observed for isothermal and adiabatic operational regimes. The influence of air number, specific catalyst area, anode thickness, steam to carbon (s/c) ratio of the inlet fuel, and extend of pre-reforming on cell performance is analyzed. In all cases except for the case of pre-reformed fuel, adiabatic operation results in lower performance compared to isothermal operation. It is further discussed that, though direct internal reforming may lead to cost reduction and increased efficiency by effective utilization of waste heat, the efficiency of the fuel cell itself is higher for pre-reformed fuel compared to non-reformed fuel. Furthermore, criteria for the choice of optimal operating conditions for cell stacks operating under direct internal reforming conditions are discussed.

Keywords: SOFC; Efficiency; Internal reforming; Fuel utilization; Numerical modeling

1. Introduction

Given a cell geometry, the performance of a SOFC strongly depends on the operating conditions and the inlet fuel composition. Since SOFCs offer a wide range of operating possibilities, identifying the effect of operating conditions such as air flow rate and inlet fuel composition on the efficiency and power density are critical for optimal operation of SOFCs. For example, extent of pre-reforming will affect fuel utilization and power density. On efficiency maps, operating in the region of high efficiency may result in a very low power density requiring large cell volume to deliver the required power output, while operating at high power density can lead to low efficiency [1]. Hence, the SOFC often has to be operated in a region of reasonable efficiency and power density. On the other hand, material cost can be optimized by judicious choice of catalyst loading and cell geometry. For example, an anode supported cell is a preferable choice for hydrocarbon fuels. However, the amount of catalyst loading and anode thickness for optimal performance are design parameters [2].

In an earlier study, Zhu and Kee presented a maximum efficiency analysis using a thermodynamic model [1]. They concluded that the maximum possible efficiency is independent of the characteristics of membrane electrode assembly and the internal polarization losses. A number of publications report exergy analysis of SOFC systems [3–5]. Unlike these models, the study presented here is based on a very detailed SOFC model and focuses on a unit cell. In a previous study, we presented a numerical model to simulate a planar cell under isothermal conditions [6]. The study incorporated detailed models for heterogeneous chemistry using an elementary step reaction mechanism for the steam reforming of CH_4 on nickel catalysts. Furthermore, the electrochemistry was modeled using a modified Butler–Volmer setting based on single-step electron transfer reaction. In the present study, the model presented in [6] is extended to non-isothermal conditions in order to analyze the effects of the operating variables on cell performance. Though it may be possible to run a cell under isothermal conditions in a laboratory environment, the scenario is completely different for a technical system. In general, each channel in a SOFC stack behaves

* Corresponding author.
E-mail address: deutschmann@ict.uni-karlsruhe.de (O. Deutschmann).

0378-7753/$ – see front matter © 2007 Elsevier B.V. All rights reserved.
doi:10.1016/j.jpowsour.2007.07.008

Nomenclature

A_c	area of cross section of flow channels (m^2)
A_s	specific area (m^{-1})
B_g	permeability (m^2)
C_p	specific heat ($J\,kg^{-1}\,K^{-1}$)
d_p	particle diameter (m)
D	diffusivity ($m^2\,s^{-1}$)
D_h	hydraulic diameter (m)
E_{cell}	cell voltage (V)
E_{th}	thermoneutral voltage (V)
F	Faraday number ($C\,mol^{-1}$)
Gz	Graetz number
h	heat transfer coefficient ($J\,m^{-2}\,K^{-1}\,s^{-1}$); specific enthalpy ($J\,kg^{-1}$)
H_c	channel height (m)
ΔH	enthalpy of formation ($J\,mol^{-1}$)
i	current density ($A\,cm^{-2}$)
J_k	species flux ($mol\,m^{-2}\,s^{-1}$)
k	thermal conductivity ($J\,m^{-1}\,s^{-1}\,K^{-1}$)
K_g	number of gas-phase species
$\dot{m}$	mass flux ($kg\,s^{-1}$)
n	number of charge transferred
$\dot{n}$	molar flow rate ($mol\,s^{-1}$)
Nu	Nusselt number
O_{min}	minimum O_2 required ($mol\,m^{-3}$)
p	pressure (Pa)
P_e	MEA perimeter (m)
Pr	Prandtl number
Q	Source term $(J\,(s\,m^3)^{-1})$
R	gas constant ($J\,mol^{-1}\,K^{-1}$)
Re	Reynolds number
$\dot{s}$	molar production rate ($mol\,m^{-2}\,s^{-1}$, $mol\,m^{-3}\,s^{-1}$)
ΔS	entropy change ($J\,K^{-1}$)
t	time (s)
T	temperature (K)
v	velocity ($m\,s^{-1}$)
$\bar{W}$	average molecular weight ($kg\,mol^{-1}$)
W_k	molecular weight of kth species ($kg\,mol^{-1}$)
$[X]$	concentration ($mol\,m^{-3}$)
Y	mass fraction

Greek symbols

Γ	surface site density ($mol\,cm^{-2}$)
δ	Kronecker symbol
ϵ	emissivity
η	efficiency
η_u	fuel utilization
θ	surface coverage
λ	air number
μ	viscosity ($kg\,m^{-1}\,s^{-1}$)
ρ	density ($kg\,m^{-3}$)
σ	co-ordination number; conductivity ($S\,cm^{-1}$)
τ	tortuosity
ϕ	porosity

Subscripts

c	channel
e	electrolyte/electrode
f	fluid
I	interconnect
k	species index

differently. For example, the temperature profile developing at the outer most channels in the stack can be quite different from the one located at the center of the stack. Nevertheless, it is rational to assume that the extremes of the stack behavior can be well understood by isothermal and adiabatic cases. Therefore, calculations are performed for both isothermal and adiabatic conditions. However, running detailed models like the one reported in this paper on stack level would require enormous computational time. Therefore, a single cell is analyzed in the present study.

2. Model description

In a previous publication, we reported an elliptical model to describe the transport and chemical processes within the cell [7]. However, in this paper we discuss a parabolic model to describe the operation of a planar SOFC, which reduces the computational effort of the mass and heat transport calculation. The following sections encompass the modeling framework adopted in this work. A schematic representation of the model geometry considered in this study is shown in Fig. 1.

2.1. Mass and heat transport

2.1.1. Channel flow

Flow through fuel and air channels can be assumed to be one-dimensional and laminar. Then the plug flow equation for species continuity

$$\frac{\partial(\rho_f Y_k)}{\partial t} = -\frac{\partial(\rho_f u Y_k)}{\partial z} + \frac{P_e}{A_c} J_k W_k, \quad k = 1, \ldots, K_g, \tag{1}$$

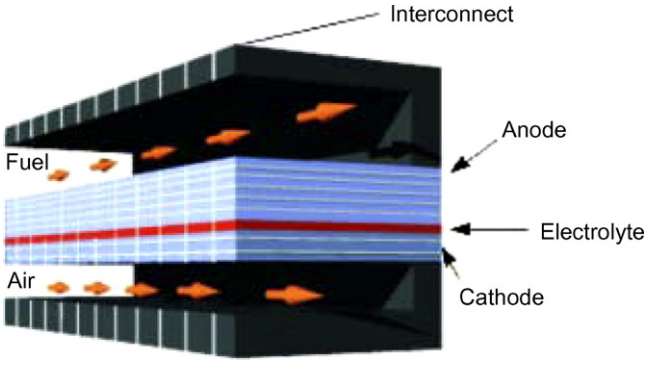

Fig. 1. A schematic representation of planar cell under consideration.

and the mass balance equation

$$\frac{\partial \dot{m}}{\partial t} = -\frac{\partial(\dot{m}u)}{\partial z} + u\sum_{k=1}^{K_g} P_e J_k W_k, \tag{2}$$

can be applied. Here ρ_f is the fluid density, Y_k the species mass fraction of species k, u the velocity, P_e the perimeter associated with the membrane electrode assembly, $\dot{m}$ the mass flux, z the axial position, t the time, and W_k is the species molecular weight. Assuming constant pressure in the channels, the density is calculated from the ideal gas equation

$$p\bar{W} = \rho_f RT. \tag{3}$$

In Eqs. (1) and (2), J_k is the flux at the electrode channel interface and is calculated using the dusty gas model (DGM) (Eq. (11)). The temperature T_f in the flow channels is determined from the heat balance equation

$$\frac{\partial(\rho_f C_{pf} T_f)}{\partial t} = -\frac{\partial(u\rho_f C_{pf} T_f)}{\partial z} - \frac{h}{H_c}(T_f - T_e) + \frac{h}{H_c}(T_I - T_f). \tag{4}$$

Here C_{pf} is the specific heat capacity of the fluid; T_f, T_e, and T_I are the temperature of fluid stream, electrode, and interconnect, respectively. The first term on the right-hand side of Eq. (4) represents the transport of energy due to the bulk fluid flow, second term represents the heat transfer from the channel to the electrode structure, and third term represents the heat transfer from the interconnect into the flow channels. The heat transfer coefficient h is evaluated from the Nusselt number

$$Nu = \frac{hD_h}{k}, \tag{5}$$

where D_h is the hydraulic diameter and k is the thermal conductivity of the fluid. The Nusselt number is expressed empirically as [8]:

$$Nu = 3.095 + 8.933\left(\frac{1000}{Gz}\right)^{-0.5386} \exp\left(-\frac{6.7275}{Gz}\right), \tag{6}$$

where the Graetz number, Gz, is given in terms of the Reynolds number, Re, and Prandtl number, Pr, as

$$Gz = \frac{D_h}{z} Re\, Pr, \tag{7}$$

where z is the axial position along the channel. Re and Pr are defined as

$$Re = \frac{D_h u\rho}{\mu} \quad \text{and} \quad Pr = \frac{C_{pf}\mu}{k}. \tag{8}$$

2.1.2. Porous media transport

Species transport through the porous media is assumed to be one-dimensional along the thickness of the porous structure and given by

$$\frac{\partial(\phi\rho_f Y_k)}{\partial t} = -\frac{\partial(J_k W_k)}{\partial y} + \dot{s}_k W_k A_s. \tag{9}$$

Here, ϕ is the porosity, $\dot{s}_k$ the heterogeneous molar production rate of the chemical species k, y the independent spatial variable along the thickness, and A_s is the specific catalyst area available for surface reactions. Total density of the fluid within the porous structure can be calculated from

$$\frac{\partial(\phi\rho_f)}{\partial t} = -\sum_{k=1}^{K_g}\frac{\partial(J_k W_k)}{\partial y} + \sum_{k=1}^{K_g}\dot{s}_k W_k A_s. \tag{10}$$

In the above equations, the fluxes J_k are evaluated using the dusty gas model (DGM). According to DGM, the net species molar flux is given by [6,9–11]

$$J_k = -\left[\sum_{l=1}^{K_g}\mathcal{D}_{kl}^{DGM}\nabla[X_l] + \left(\sum_{l=1}^{K_g}\frac{\mathcal{D}_{kl}^{DGM}[X_l]}{\mathcal{D}_{l,kn}^{e}}\right)\frac{B_g}{\mu}\nabla p\right]. \tag{11}$$

The first term on the right-hand side of Eq. (11) represents the diffusive flux and the second term represents the viscous flux. $\mathcal{D}_{kl}^{DGM}$ are defined as DGM diffusion coefficients given as [6]

$$\mathcal{D}_{kl}^{DGM} = H^{-1}, \tag{12}$$

where the elements of H matrix are

$$h_{kl} = \left[\frac{1}{\mathcal{D}_{k,kn}^{e}} + \sum_{j\neq k}\frac{X_j}{\mathcal{D}_{kj}^{e}}\right]\delta_{kl} + (\delta_{kl} - 1)\frac{X_k}{\mathcal{D}_{kl}^{e}}. \tag{13}$$

The permeability B_g in Eq. (11) is given by the Kozeny–Carman relationship [12]:

$$B_g = \frac{\phi^3 d_p^2}{72\tau(1-\phi)^2}. \tag{14}$$

Here d_p is the particle diameter and τ is the tortuosity. Assuming the reaction heat is released on the solid surface the heat balance equation within the porous structure can be written as

$$\frac{\partial(\rho C_p T)}{\partial t} = \nabla\cdot(k_{eff}\nabla T) - \sum_{k=1}^{K_g}\dot{s}W_k A_s h_k \tag{15}$$

Here, ρ is the density of the solid structure, C_p the specific heat capacity of the solid structure, and k_{eff} is the effective thermal conductivity. The first term on the right-hand side represents heat transfer due to conduction and the second term represents the heat release due to heterogeneous reactions within the electrodes. Three source terms, Q_r, Q_h, and Q_e, enter as the boundary condition for Eq. (15). The radiative heat transfer between the interconnect and the outer most discretized cell in the porous electrode is given by

$$Q_r = \frac{1}{\delta y}\left[\frac{\sigma\left(T_I^4 - T^4\right)}{(1/\epsilon_I) + (1/\epsilon) - 1}\right], \tag{16}$$

where ϵ_I and ϵ represent the emissivity of the interconnect and the electrode, respectively. The convective heat transfer between the fluid in the channel and the outer most discretized cell in the porous electrode is given by

$$Q_h = \frac{h}{\delta y}(T_f - T). \tag{17}$$

δy appearing in Eqs. (16) and (17) results from the finite volume integration over the discretized cells and must have a finite value. Q_e arises from the electrochemical heat release at the three-phase boundary (Eq. (19)). The global charge transfer reaction at the three-phase interface can be written as

$$H_2 + O^{2-} \rightarrow H_2O + 2e^-, \tag{18}$$

however, only a part of the energy change during the reaction is released as heat, that amounts to

$$Qe = -\frac{T\Delta S}{\delta y}\frac{i}{2F}. \tag{19}$$

Assuming the electrolyte to be one-dimensional the heat balance equation is reduced to

$$\frac{\partial\left(\rho C_p T\right)}{\partial t} = \frac{\partial}{\partial z}\left(k\frac{\partial T}{\partial z}\right) + \frac{i^2}{\sigma_e}. \tag{20}$$

The last term in the above equation represents the ohmic heating due to ion transport in the electrolyte. Though the electrodes and interconnects also contribute to ohmic heating due to electronic resistance, their contribution is minor compared to the ionic resistance offered by the electrolytes and is neglected in the present study.

2.1.3. Interconnect

The heat balance equation for the interconnect can be summarized as

$$\frac{\partial(\rho C_{pI} T_I)}{\partial t} = \frac{\partial}{\partial z}\left(k\frac{\partial T_I}{\partial z}\right) + \frac{h}{H_I}(T_f - T_I) - \frac{1}{H_I}\left[\frac{\sigma\left(T_I^4 - T^4\right)}{(1/\epsilon_I) + (1/\epsilon) - 1}\right]. \tag{21}$$

Here, C_{pI} is the specific heat capacity, and ρ is the density of the interconnect material. The first term on the right-hand side represents the conduction within the interconnect, second and third terms represent the heat transferred to/from the channel to interconnect and the radiation transfer to/from the interconnect to the electrode structure.

Eqs. (15), (20), and (21) require boundary conditions at $z = 0$ and $z = L$ given by

$$\left.\frac{\partial T}{\partial z}\right|_{z=0} = 0, \qquad \left.\frac{\partial T}{\partial z}\right|_{z=L} = 0. \tag{22}$$

Modeling radiative heat transfer in SOFCs is a complex process and the radiative transport within the semitransparent electrodes and electrolyte as well as surface to surface heat transfer must be accounted for an accurate calculation. However, an exact knowledge of phenomenological properties like absorption coefficient, refractive index, scattering coefficient, emissivity, and reflectivity is not available and hence represents an obstacle in modeling radiative heat transport in SOFC electrodes and electrolyte. A detailed discussion of radiation heat transfer in SOFC is given elsewhere [13–16]. In an analysis of spectral radiation in SOFC electrodes, Damm and Fedorov [14] proved that the radiation effects in SOFC electrodes are minimal and can safely be neglected. Therefore, in the present work, we only consider surface to surface radiation. Since the planar geometry considered here is of high aspect ratio ($L/d > 50$) the surfaces can be treated as black bodies with unity emissivity [13].

2.2. Heterogeneous chemistry and electrochemistry

The anode chemistry model adopted here excerpts the potential of elementary heterogeneous mechanism for the steam reforming of methane on Ni catalysts. The modeling framework of heterogeneous chemistry is described in our previous reports [6,7,17]. The relation between surface coverages θ_k and the surface concentrations $[X_k]$ is given by

$$\theta_k = \frac{[X_k]\sigma_k}{\Gamma}, \tag{23}$$

and the temporal variations of surface coverages are given by

$$\frac{d\theta}{dt} = \frac{\dot{s}_k\sigma_k}{\Gamma}, \quad k = K_g + 1, \ldots, K_g + K_s, \tag{24}$$

where $\dot{s}_k$ is the surface reaction rate, σ_k the co-ordination number (number of sites required for a species for adsorption), Γ the surface site density, and K_s is the number of surface species [7,17,6].

Assuming H_2 as the only electrochemically active species and neglecting the contribution by CO, the electrochemistry model is implemented using a modified Butler–Volmer setting based on single-step electron transfer mechanism, and is described in detail in our previous report [6]. Neglecting the contribution by CO is a safe assumption due to the low electrochemical activity of CO compared to H_2 when both are present together in the system [18]. The activation energy and pre-exponential factor in the expression for the exchange current density for hydrogen oxidation and oxygen reduction are taken from [7]. Since the chemistry and electrochemistry models are discussed thoroughly in our previous reports, they are not a subject of further discussion here. However, we ascertain here that the heterogeneous chemistry mechanism is not validated for carbon deposition conditions.

2.3. Efficiency model

There are many discussions in the literature on the efficiency analysis of fuel cells [1,19–21]. The efficiency of a cell is usually expressed in terms of cell voltage, fuel utilization, and the thermoneutral voltage [22]

$$\eta = \eta_u\frac{E_{cell}}{E_{th}}. \tag{25}$$

Here, η_u is the fuel utilization, E_{cell} the operating cell voltage, and E_{th} is the thermoneutral voltage. The fuel utilization,

$$\eta_u = \frac{W\int_0^L i\,dx}{\dot{n}_{fuel}nF} \tag{26}$$

depends on the operating voltage, fuel and air flow rates, available specific area for internal reforming, and the cell geometry [22]. In the above equation, W is the width associated with the

Table 1
Cell geometry and operating conditions for various cases under consideration

Case	Length (cm)	Fuel inlet condition 800 °C			Air number	Comments
		CH_4%	H_2O%	u (cm s^{-1})		
(a)	10	40	60	30	Variable	–
(b)	10	40	60	30	1	Variable anode thickness
(c)	10	–	–	30	3	Variable s/c ratio
(d)	10	40	60	30	1	–
(e)	5	–	–	30	5	Air inlet at 600 ° C and various levels of pre-reforming

MEA and $\dot{n}_{\text{fuel}}$ is the molar flow rate of the fuel. The thermoneutral voltage is defined as

$$E_{\text{th}} = \frac{\Delta H}{nF}, \tag{27}$$

where ΔH is the enthalpy of formation, and n is the total number of electrons transferred.

3. Computational procedure

In order to solve the equation systems they are first cast into a finite volume form. The channels, interconnects, and electrolyte are treated as one-dimensional, and the reactor geometry is discretized in the axial direction into 200 cells. The anode is discretized into 25 cells along the thickness and the cathode into 10 cells. Eqs. (1)–(4), (9), (10), (15), (20), (21), and (24) form a system of coupled non-linear equations which can be written in the residual form as

$$F(\Phi) = 0, \tag{28}$$

where the vector Φ is given by

$$\Phi = [(T)_{\text{ic}}, (Y, \dot{m}, T)_{\text{f}}, (Y, \rho, T, \theta)_{\text{a},1}, \ldots, (Y, \rho, T, \theta)_{\text{a,n}}, (T)_{\text{e}}, (Y, \rho, T)_{\text{c},1}, \ldots, (Y, \rho, T)_{\text{c,m}}, (Y, \dot{m}, T)_{\text{a}}, (T)_{\text{ic}}]^T. \tag{29}$$

Here the indexes (ic),(f),(a,1),(a,n),(e),(c,1),(c,m),(a) stand for interconnect, fuel channel, first discretized cell in the anode, nth discretized cell in the anode, electrolyte, first discretized cell in the cathode, mth discretized cell in the cathode, and air channel, respectively. The entire solution procedure follows a space marching algorithm. At each axial position the transient system of equations are solved until a steady state solution is obtained. The initial condition at each axial position assumes the converged solution from the previous finite volume cell. Due to the elliptic nature of heat balance equation in porous electrodes and the conductive terms in the solid regions, an outer iteration loop is formed around the marching algorithm. The equation system is solved using the differential algebraic equation (DAE) solver LIMEX [23]. The entire solution converges in few passes.

4. Results and discussion

The effect of various parameters on cell performance is studied systematically. The study covers the effect of (a) air flow rate, (b) anode thickness, (c) steam to carbon ratio of the fuel, (d) specific area available for surface reactions, and (e) extend of pre-reforming on cell efficiency and power density. In all cases, computations are performed for adiabatic as well as isothermal operations. For adiabatic calculations the outer interconnect walls are assumed to be adiabatic, i.e., no heat transfer over the interconnects. All isothermal calculations are carried out for a constant temperature of 800 °C. Furthermore, in all cases the cell is assumed to operate at a constant voltage of 0.7 V. Table 1 lists conditions used for the various cases studied and the membrane electrode assembly (MEA); parameters are given in Table 2. In all cases, the fuel stream consisting of 40 vol.% $CH_4$and 60

Table 2
MEA parameters for all simulations

Parameters	Values	Units
Anode		
Thickness (l_a)	0.75	mm
Width (W_a)	1.00	mm
Average pore radius (r_p)	0.50	μm
Average particle diameter (d_p)	2.50	μm
Specific area (A_s)	1025.00	cm^{-1}
Porosity (ϵ)	0.35	
Tortuosity (τ)	3.80	
Charge transfer coefficient (β_a)	0.50	
Specific heat (C_{pI})	450.00	J kg^{-1} K^{-1}
Density	3310.00	kg m^{-3}
Thermal conductivity (k)	1.86	J m^{-1} s^{-1} K^{-1}
Electrolyte		
Thickness (l_e)	25.00	μm
Width (W_e)	1.00	mm
Specific heat (C_{pe})	470.00	J kg^{-1} K^{-1}
Density	5160.00	kg m^{-3}
Thermal conductivity (k)	2.16	J m^{-1} s^{-1} K^{-1}
Cathode		
Thickness (l_c)	30.00	μm
Width (W_c)	1.00	mm
Average pore radius (r_p)	0.50	μm
Average particle diameter (d_p)	2.50	μm
Porosity (ϵ)	0.35	
Tortuosity (τ)	3.80	
Charge transfer coefficient (β_a)	0.50	
Specific heat (C_p)	430.00	J kg^{-1} K^{-1}
Density	3030.00	kg m^{-3}
Thermal conductivity (k)	5.84	J m^{-1} s^{-1} K^{-1}
Interconnect		
Thickness (l_i)	300.00	μm
Specific heat (C_{pI})	550.00	J kg^{-1} K^{-1}
Density	3030.00	kg m^{-3}
Thermal conductivity (k)	20.00	J m^{-1} s^{-1} K^{-1}

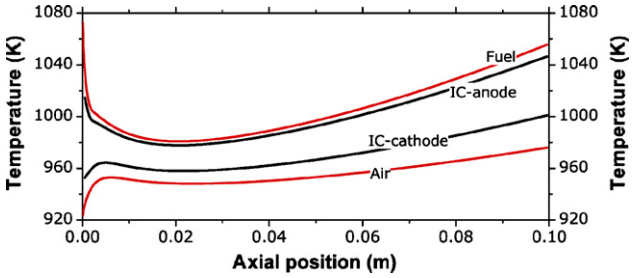

Fig. 2. Temperature profile within flow channels and interconnects for a cell operating at 0.7 V. Air stream is assumed to enter the cathode channel at 650 °C. The cell is assumed to operate under adiabatic conditions.

vol.% H_2O is assumed to enter the cell at 800 ° C with a velocity of 30 cm s^{-1}.

The temperature distributions in the fuel/air channels and the interconnects are shown in Fig. 2. Interestingly, the anode side interconnects are at lower temperature than the fuel temperature; nonetheless, the cathode side interconnects are at higher temperature than the air temperature. The increased temperature of cathode side interconnect compared to the air temperature is primarily due to the heat radiation from the cathode electrode to the interconnect. Near the inlet, the fuel stream transfers heat to the relatively cold air entering the cathode, further heat is consumed by the endothermic reforming reactions.

The temperature distributions within the anode and cathode are presented in Fig. 3(a) and (b). The decrease of temperature near the fuel inlet due to reforming also affects fuel utilization. For direct internal reforming longer cells are required to achieve better fuel utilization. The fuel and air utilization for the case shown in the Fig. 3(a) and (b) are 57.5% and 24%, respectively. The temperature increase downstream the channel is primarily due to the exothermic cell reactions; overpotential losses, shift reactions, and the charge transfer reactions are exothermic. There is a general notion that internal reforming leads to temperature drop near the cell inlet. However, the position of the reforming zone is determined by the inlet fuel velocity/flow rate. Fig. 4 demonstrates the influence of fuel inlet velocity on the position of reforming zone. In the case of 30 cm s^{-1} the reforming zone is 2 cm down the fuel inlet. However, for the

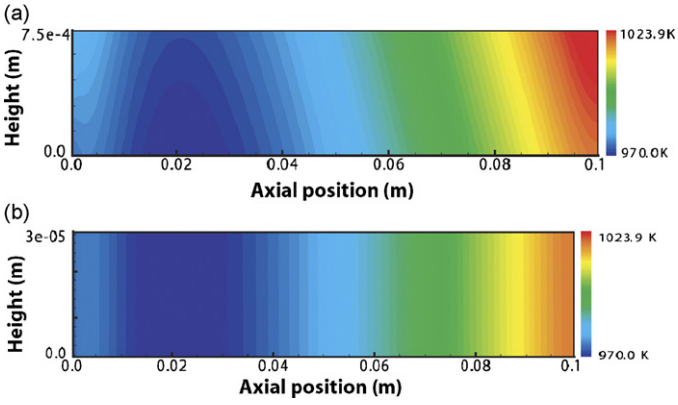

Fig. 3. Temperature distribution within the anode and cathode for a cell operating at 0.7 V under adiabatic conditions. Air stream is assumed to enter the cathode channel at 650 °C: (a) anode and (b) cathode.

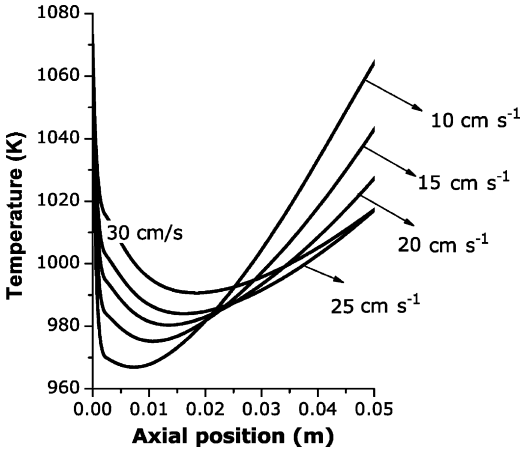

Fig. 4. Influence of the inlet velocity on the position of reforming zone.

case of 10 cm s^{-1} the reforming zone if 5 mm down the fuel inlet.

For an adiabatic case, the species distributions within the fuel channel and the anode are shown in Fig. 5. The top panel displays the species distribution along the fuel channel, while the drop down panels depict the profiles across the anode thickness at selected axial positions. The reforming chemistry within the cell produces H_2 and CO by consuming CH_4 and H_2O. Although the concentration of H_2O initially decreases due to reforming, the electrochemical production of H_2O leads to further increase downstream the cell. The concentration of H_2 gradually drops as a result of electrochemical consumption. Although, CO can participate in charge transfer reactions, in the analysis carried out here, H_2 is considered to be the only electrochemically active species. Therefore, any CO produced participates either in shift reaction or in Bouduard reaction.

Fig. 6 displays the surface coverages of surface adsorbed species. The bottom panel shows the coverages along the three-phase boundary. The surface coverage of oxygen decreases initially and increases further down the length of the reactor, following the trend of H_2O concentration in the gas-phase. This is an indication that the surface coverage of oxygen results from the dissociative adsorption of H_2O. Most of the surface is covered by hydrogen and CO. The hydrogen coverage near the three-phase boundary initially increases and then drops. The increase in hydrogen coverage near the inlet is as a result of low electrochemical consumption due to the temperature drop near the inlet. This conclusion is supported by the profile of current density along the length of the channel, where the current density decreases as a result of temperature decrease (Fig. 7). Though the mechanism is ineffective in predicting the carbon deposition quantitatively, qualitative agreement with experimental observations has been reported previously [7].

Though the results show negligible carbon deposition it should be kept in mind that the chemistry mechanism used here is not particularly validated for carbon deposition conditions. Downstream in the channel, the free Ni surface area increases possibly due to increasing desorption rate with increasing temperatures and due to the consumption of CO and H_2 by shift and electrochemical reactions. The drop up panels

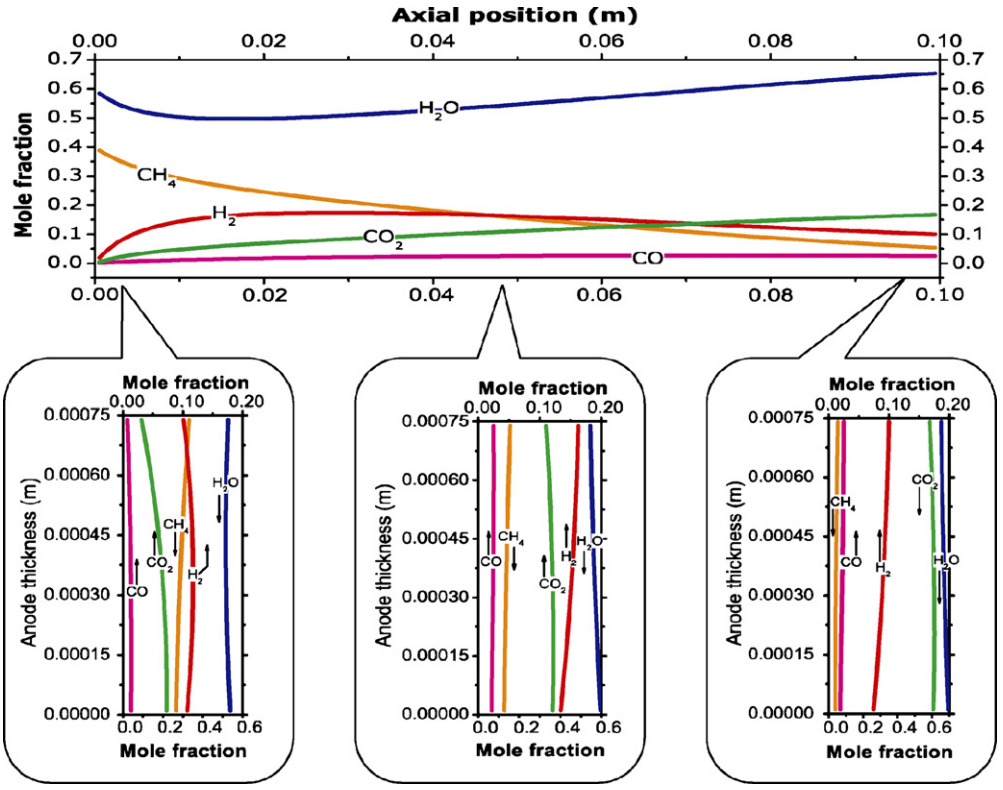

Fig. 5. Species profiles within the fuel channel and anode. The drop down panels shows the species profiles across the anode thickness at various axial positions. The anode considered is 750 μm thick and the inlet fuel enters at 800 °C, while air is assumed to enter at 650 °C.

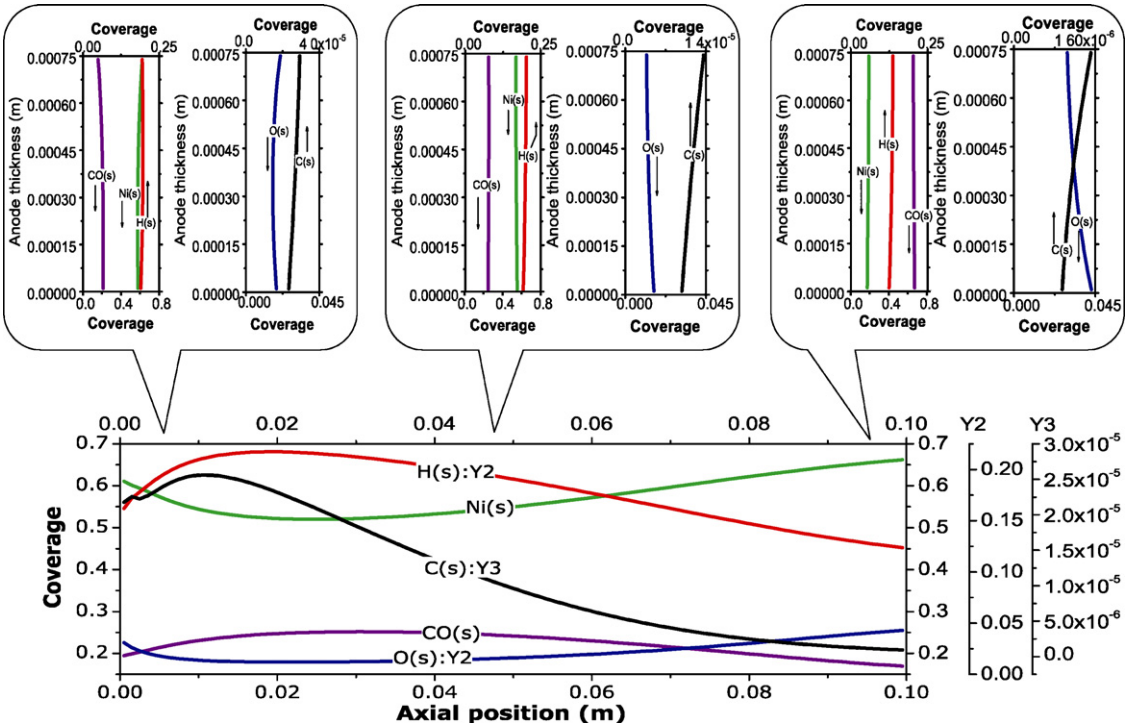

Fig. 6. Surface coverages of major adsorbed species. The drop down panels shows the species profiles across the anode thickness at various axial positions. The anode considered is 750 μm thick and the inlet fuel enters at 800 °C, while air is assumed to enter at 650 °C. The bottom panel shows the coverages along the three-phase boundary and the top panels display the coverages across the anode thickness.

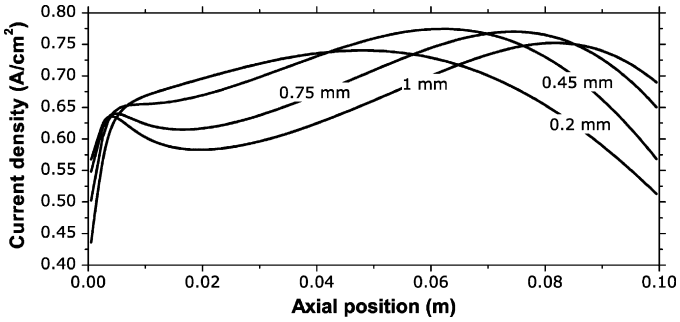

Fig. 7. Current density as a function of the axial position for various anode thicknesses. Air enters the cathode channel at 650 °C, λ = 1.

present the coverages across the anode thickness at selected axial positions.

4.1. Air flow rate

Maintaining high air flow rates to keep the cell temperature within the limits of durable electrode performance is essential for long term operation of SOFCs. However, the amount of excess air required depends on the inlet fuel composition. For example, an internally reforming cell requires less excess air than a cell operating on pure hydrogen fuel. However, it is well known that high operating temperature results in better cell performance, and hence an inordinate excess air flow rate can dramatically reduce the cell performance by lowering the average cell temperature. Therefore, choosing the amount of excess air, resulting in an optimum balance between cell performance and cell durability is critical.

In the calculations carried out here, excess air is defined in terms of air number λ defined as

$$\lambda = \frac{\dot{n}_{\text{air}}}{\dot{n}_{\text{fuel}} L_{\text{min}}}, \tag{30}$$

where

$$L_{\text{min}} = \frac{O_{\text{min}}}{[X]^{\text{o}}_{\text{O}_2}}. \tag{31}$$

In the above equations, $\dot{n}_{\text{fuel}}$ is the molar flow rate of the fuel stream, O_{min} is the minimum O_2 concentration required for the complete oxidation of the inlet fuel and $[X]^{\text{o}}_{\text{O}_2}$ is the concentration of O_2 in the cathode stream.

Fig. 8 shows the efficiency and power density as a function of air number (Eq. (30)). Fuel and air streams are assumed to enter the cell at 800 and 650 °C, respectively. It is quite apparent from Fig. 8 that both efficiency and power density decrease with increasing air flow rate, because in the case of adiabatic operation an increase in air flow rate decreases the overall cell temperature resulting in reduced average current density and hence decreased fuel utilization. The gradient as well as the maximum and the minimum temperature of the solid are shown in Fig. 9.

However, the trend reverses when the cell is operated isothermally (Fig. 10). In this case both efficiency and power density increase because of the reduced air depletion with an increasing air flow rate. Furthermore, isothermal operation results in higher efficiency and power density compared to non-isothermal case.

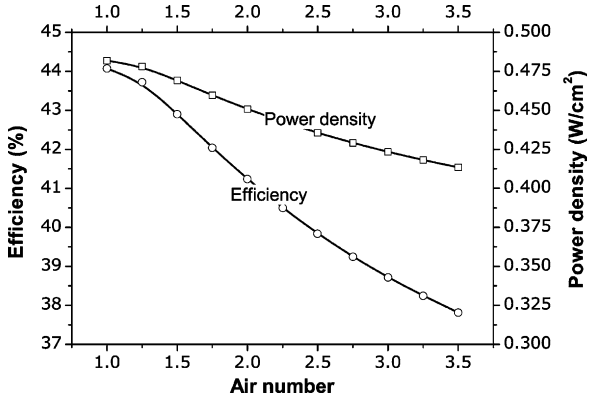

Fig. 8. Efficiency and power density for adiabatic condition as a function of air number. Cathode inlet stream (air) enters at 650 °C.

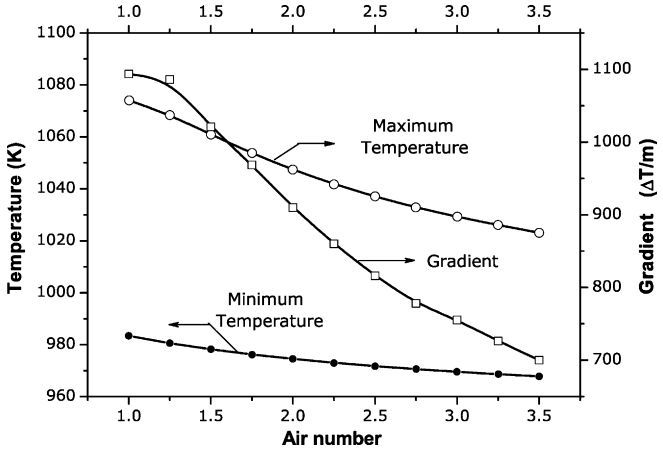

Fig. 9. Maximum, minimum, and temperature gradient of the solid for varying air flow rate to fuel flow rate; air number according to Eq. (30).

The maximum efficiency for non-isothermal operation is 44%, while isothermal operation results in a maximum efficiency of 59%. It should be noticed that under constant operating potential (0.7 V) and inlet fuel compositions, the vital factor governing power density and efficiency is the fuel utilization defined by Eq. (26). Therefore, in an operating stack each cell can lead to different levels of fuel utilization and hence different effi-

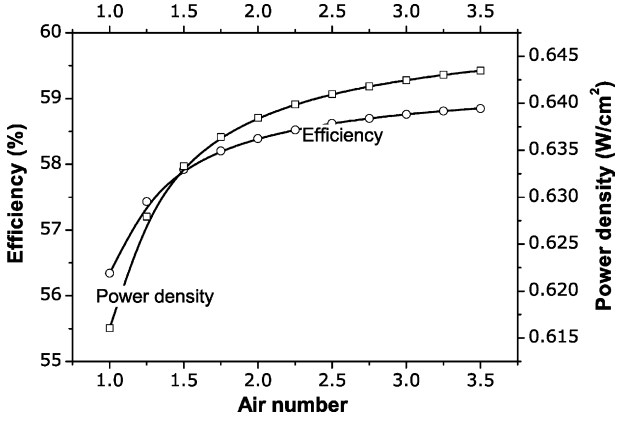

Fig. 10. Efficiency and power density for isothermal condition (800 °C) as a function of air number.

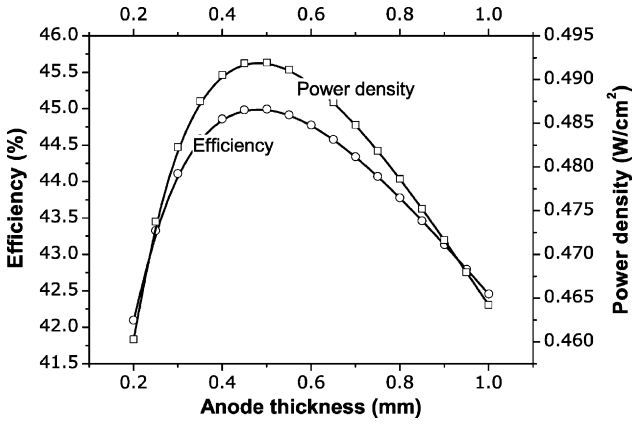

Fig. 11. Effect of anode thickness on efficiency and power density for a cell operating under adiabatic conditions. Cathode inlet is assumed to be air at 650 °C.

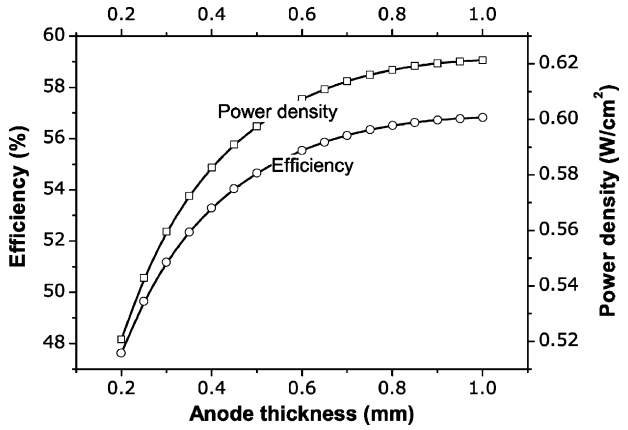

Fig. 12. Effect of anode thickness on efficiency and power density for a cell operating under isothermal conditions.

ciency levels depending on the temperature distribution, which strongly depends on the cell's position within the stack and the temperatures of the adjacent cells.

4.2. Anode thickness

Though SOFC can be either anode, electrolyte, or cathode supported, in the case of cells running on hydrocarbon fuels, anode supported cells may be preferable due to the potential for internal reforming. However, finding the optimal anode thickness required to support the cell mechanically and to achieve the desired level of internal reforming and optimal cell performance is a rather difficult task.

Fig. 11 displays the influence of the anode thickness on efficiency and power density for a cell operating under adiabatic conditions. Quite surprisingly the model predicts an optimal anode thickness at ∼0.5 mm maximizing the efficiency and power density. In every case, the fuel has to undergo internal reforming to produce H_2 and CO which further participate in the charge transfer reactions at the three-phase boundary. However, in the case of thin anodes the short diffusion path (∼0.2–0.4 mm) available for the fuel before reaching the three-phase boundary limits the amount of H_2 and CO produced by internal reforming and, hence, leads to a low average current density, efficiency, and power density. As the thickness increases, the possibility for the fuel to undergo reforming to produce H_2 and CO also increases. However, the higher extend of internal reforming achieved from the longer diffusion path also leads to larger temperature drops close to the channel inlet and hence results in decreased performance. Thus, there turns out to be an optimal anode thickness where the efficiency and power density reaches a maximum. However, it should be noticed that the optimum thickness can vary with the operating conditions, such as fuel composition, inlet temperature, velocity, catalyst loading, etc.

Fig. 12 presents the efficiency and power density as a function of anode thickness for the case of a cell operated isothermally. In this case, both efficiency and power density increase with increasing anode thickness, however, reaches an asymptotic behavior at higher anode thicknesses. This clearly indicates that even in the case of isothermal operation increasing the anode thickness beyond the optimal value does not bring any further increase in performance. Nevertheless, isothermal operation results in better performance than adiabatic operation. A maximum efficiency of 59% is achievable with isothermal operation, while the maximum possible efficiency in the case of adiabatic operation is 45%.

4.3. Steam to carbon ratio

It is quite well known that Ni based anodes are prone to coking while running on hydrocarbon fuels [24–26]. Therefore, it is quite important to have enough steam present in the inlet fuel to suppress coking. Figs. 13 and 14 respectively present the influence of steam to carbon (s/c) ratio on the performance of an adiabatically and isothermally operating cell. In both cases, the efficiency improves with increasing steam content in the inlet fuel stream, while the power density decreases with increasing steam content. The decrease in power density is due to the fuel dilution effect; diluted fuel results in a lower average current density and for the cases studied here power density solely depends on the current density due to the constant operating voltage.

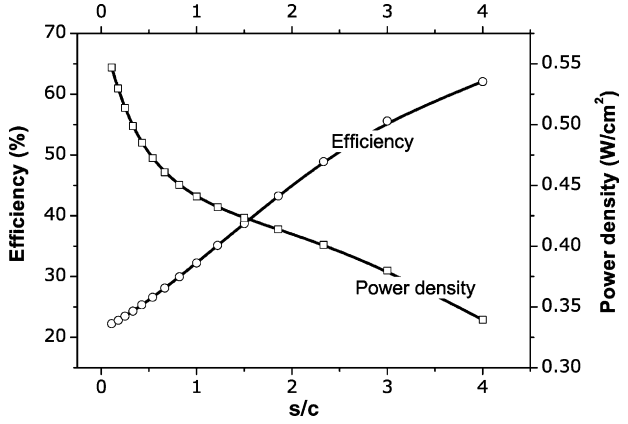

Fig. 13. Efficiency and power density for varying steam to carbon (s/c) ratio in the inlet fuel stream for a cell operating adiabatically. For all s/c ratio the fuel is assumed to enter at 800 ° C and air at 650 °C.

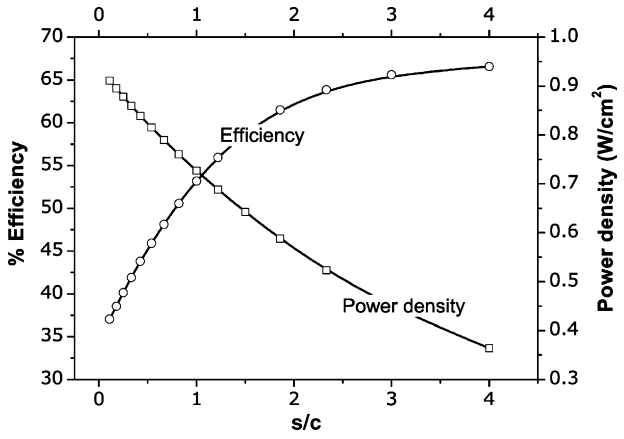

Fig. 14. Efficiency and power density for varying steam to carbon ratio (s/c) in the inlet fuel stream for a cell operating isothermally at 800°C. For call cases, the cathode stream is assumed to be air.

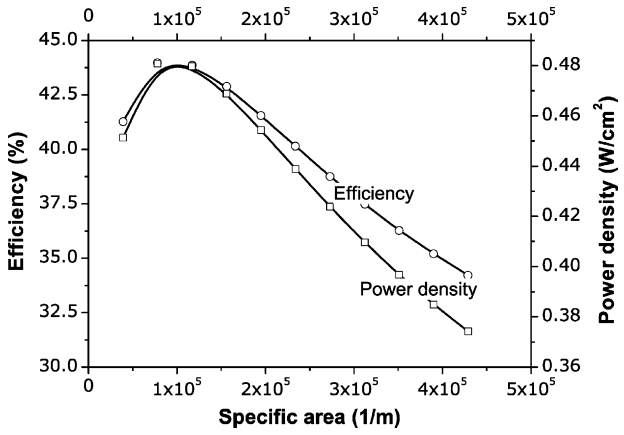

Fig. 16. Effect of specific area on efficiency and power density for cell operating adiabatically. Inlet fuel enters at 800 °C, and the air stream is assumed to enter the cathode at 650 °C.

Though the average current density decreases, the efficiency increases with increasing steam content. This is essentially counter intuitive. One would expect decreasing efficiency with increasing steam dilution, which is certainly true for the case of maximum efficiency analysis. However, one should notice that the analysis carried out here is for a particular cell geometry, and the fuel utilization for a particular cell depends on the cell dimensions. From the definition of efficiency (Eq. (25)) it is evident that for a given cell potential, efficiency strongly depends on the fuel utilization, because the thermoneutral voltage E_{th} is always ∼1.2 V. At low s/c ratios the stoichiometric current is much higher than the average current delivered by the cell leading to low fuel utilization and hence low efficiency. However, as the fuel dilution increases the stoichiometric current approaches the delivered current resulting in increased fuel utilization and hence efficiency. Fig. 15 shows the stoichiometric current and average current for the case of a cell operated at 800 °C.

Here, like in the cases mentioned above isothermal operation results in improved cell performance. In the case of higher s/c ratio a higher efficiency resulting from the higher fuel utilization leads to reduced power density, which would require large cell areas to draw the required volumetric power density. On the other hand, operating conditions providing high power density result in a very low efficiency. Therefore, a judicious choice of steam dilution has to be made to optimize power density and efficiency.

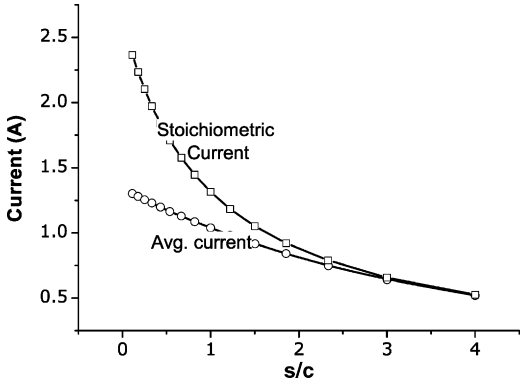

Fig. 15. Average current and stoichiometric current for varying steam to carbon ratio.

4.4. Specific area

Sufficient catalytically active surface area is needed for heterogeneous reactions. In literature, the amount of catalyst used in the anode usually is expressed in terms of weight percentage (wt%). However, from chemisorption measurements of sample anodes, it is possible to retrieve information on the available active surface area. A large catalytically active surface area results from higher catalyst loading, better catalyst dispersion, and better microstructural properties of the electrode. Fig. 16 shows the effect of specific area (area/volume) on the cell performance for a cell operated adiabatically. Both efficiency and power density are found to attain a maximum value at an available specific area of $\sim 1 \times 10^5$ m^{-1}. Large amount of catalysts can lead to excessive reforming, thereby decreasing the temperature near the inlet of the cell, resulting in a decreasing performance. A poor availability of catalytically active area results in lower production of synthesis gas participating in the charge transfer reactions, and hence resulting in a lower average current density. However, in the case of isothermal operation, both power density and efficiency are found to increase with increasing specific area (Fig. 17) and reaches an asymptotic behavior at higher values. Therefore, even in the case of isothermal operation, there is an optimal value for specific area beyond which there is no additional benefit by increasing the catalyst loading or dispersion. Nevertheless, isothermal operation results in better efficiency and power density compared to adiabatic operation.

4.5. Pre-reforming

Though the focus of this paper is on direct internal reforming, the existing applications use some extend of pre-reformed fuel. Therefore, a systematic study to understand the influence of non-reformed and pre-reformed fuels on cell efficiency is carried out. In the case considered here the non-reformed fuel is

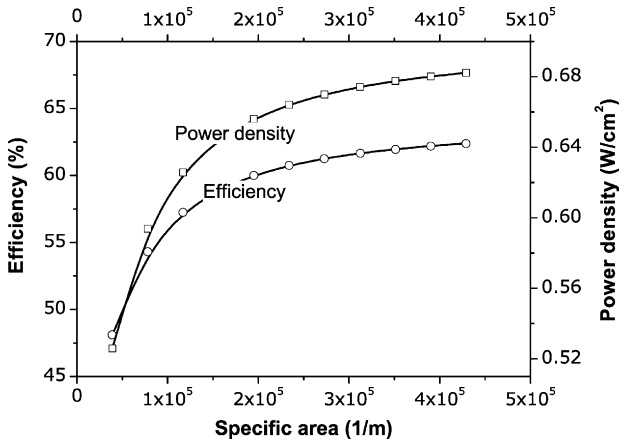

Fig. 17. Effect of specific area on efficiency and power density under isothermal condition (800 °C).

assumed to consist of 60 vol.% CH_4 and 40 vol.% H_2O; 40% pre-reforming means 40% CH_4 converted in the pre-reformer. It is expected that direct internal reforming can result in reduced cost and increased overall efficiency of the system and can also help to resolve the temperature distribution problem in the cell. However, it is quite convincing from Fig. 18 that the efficiency of the fuel cell is higher for pre-reformed fuel. Both efficiency and power density increase with extent of pre-reforming for both adiabatic and isothermal case (Fig. 19). Unlike other cases, adiabatic operation results in better performance of the cell with increasing extent of pre-reforming. For example, with 60% pre-reforming, adiabatic operation results in ~45% efficiency, while isothermal operation results in ~42% efficiency. However, with the lowest extend of pre-reforming considered here (20%), adiabatic operation results in lower efficiency and power density than isothermal operation. With increasing extent of pre-reforming, the H_2 content of inlet fuel increases, resulting in higher cell temperatures leading to higher performance, while the non-reformed fuel results in internal reforming leading to temperature drop and hence lower power density and efficiency. Furthermore, due to the short reactor length considered here, the fuel utilization

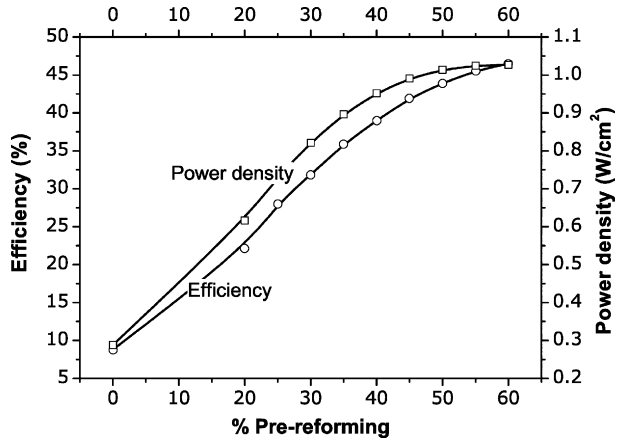

Fig. 18. Effect of pre-reforming on efficiency and power density under adiabatic condition. In call cases the pre-reformed fuel is assumed to enter at 800 ° C and air at 600 °C. The non-reformed fuel is assumed to be 60 vol.% CH_4 and 40 vol.% H_2O.

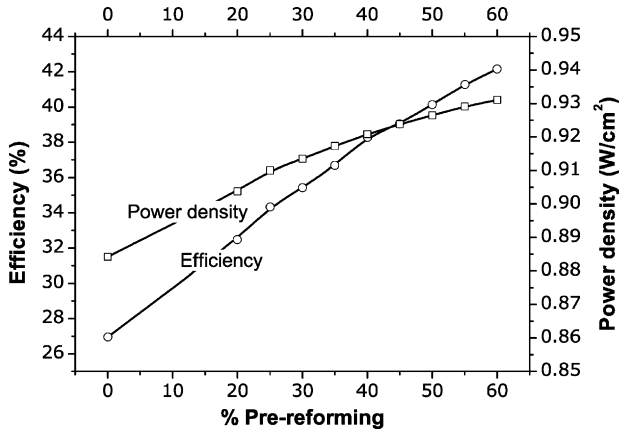

Fig. 19. Effect of pre-reforming on efficiency and power density under isothermal condition (800 °C). The non-reformed fuel is assumed to be 60 vol.% CH_4 and 40 vol.% H_2O.

efficiency turns out to be lower for non-reformed fuel. This also leads to a lower overall efficiency. However, it should be noticed that with increasing levels of pre-reforming, increasing amounts of excess air to keep the cell temperature within the limits would be required, and the system should be designed to utilize the waste heat produced by the cell.

5. Conclusions

Based on detailed models of transport and chemistry we have systematically analyzed the effect of various parameters on cell performance for a particular SOFC geometry. The vital factor for optimal cell performance has been found to be the resulting temperature profile within the cell. Judicious choice of steam dilution of the inlet fuel has to be made, that can well suppress the coking, while achieving reasonable efficiency and power density. As a remarkable outcome, excessive amount of catalysts and highly thick anodes have been found to have detrimental effect on cell performance in the case of direct internal reforming under adiabatic conditions. Even for the case of isothermal operation optimal values exists for anode thickness and active specific area. Furthermore, though direct internal reforming is known to increase the overall efficiency of the system, the efficiency of the fuel cell itself is found to be higher for the case of pre-reformed fuel. In all cases, except for the case of pre-reformed fuel, isothermal conditions resulted in better cell performance. Therefore, in the case of direct internal reforming, it is quite important to have the cell designed in a way to achieve more or less isothermal operation of the stack, which can result in higher performance.

Acknowledgment

We gratefully acknowledge many fruitful discussions with Professor R.J. Kee and Dr. H. Zhu at Colorado School of Mines.

References

[1] H. Zhu, R.J. Kee, J. Power Sources 161 (2006) 957–964.

[2] Y. Jiang, A.V. Virkar, J. Electrochem. Soc. 150 (2003) A942–A951.
[3] S.H. Chann, C.F. Low, O.L. Ding, J. Power Sources 103 (2002) 188–200.
[4] N. Hotz, S.M. Senn, D. Poulikakos, J. Power Sources 158 (2006) 333–347.
[5] S. Douvartzide, F. Coutelieris, P. Tsiakaras, J. Power Sources 131 (2004) 224–230.
[6] H. Zhu, R.J. Kee, V.M. Janardhanan, O. Deutschmann, D.G. Goodwin, J. Electrochem. Soc. 152 (2005) A2427–A2440.
[7] V.M. Janardhanan, O. Deutschmann, J. Power Sources 162 (2006) 1192–1202.
[8] R.E. Hayes, S.T. Kolaczkowski, Introduction to Catalytic Combustion, Gordon and Breach Science Publishers, Amsterdam, 1997.
[9] R. Krishna, Chem. Eng. J. 35 (1987) 75–81.
[10] R. Jackson, Transport in Porous Catalysts, Elsevier, Amsterdam, 1977.
[11] E.A. Mason, A.P. Malinauskas, Gas Transport in Porous Media. The Dusty Gas Model, Elsevier, Amsterdam, 1983.
[12] J. Baer, Dynamics of Fluids in Porous Media American, Elsevier, New York, 1972.
[13] D.L. Damm, A.G. Fedorov, J. Power Sources 143 (2005) 158–165.
[14] D.L. Damm, A.G. Fedorov, ASME 2 (2005) 258–262.
[15] S. Murthy, A.G. Fedorov, J. Power Sources 124 (2003) 453–458.
[16] J.D.J. VanderSteen, J.G. Pharoah, ASME 62 (2006) 62–67.
[17] E.S. Hecht, G.K. Gupta, H. Zh, A.M. Dean, R.J. Kee, L. Maier, O. Deutschmann, Appl. Catal. A. Gen. 295 (2005) 40–51.
[18] A.M. Sukeshini, B. Habibzadeh, B.P. Becker, C.A. Stoltz, B.W. Eichhorn, G.S. Jackson, J. Electrochem. Soc. 153 (2006) A705–A715.
[19] A. Rao, J. Maclay, S. Samuelsen, J. Power Sources 134 (2004) 181–184.
[20] A.E. Lutz, R.S. Larson, J.O. Keller, Int. J. Hydrogen Energy 27 (2002) 1103–1111.
[21] K.T. Jacob, S. Jain, in: S.C. Singhal, J. Mizusaki (Eds.), Solid Oxide Fuel Cells IX (SOFC-IX), vol. 1, 2005, pp. 629–639.
[22] J. Hartvigsen, S. Elangovan, A. Khandkar, in: P. Stevens (Eds.), Proceedings of the 3rd European Solid Oxide Fuel Cell Forum, Nantes-France, 1998, pp. 517–524.
[23] P. Deuflhardt, E. Hairer, J. Zugk, Numer. Math. 51 (1987) 501–516.
[24] J.H. Koh, Y.S. Yoo, J.W. Park, H.C. Lim, Solid State Ionics 149 (2002) 157–166.
[25] C.M. Finnerty, N.J. Coe, R.H. Cunningham, R.M. Ormerod, Catal. Today 46 (1998) 137–145.
[26] S. McIntosh, H. He, S. Lee, O.C. Nunes, V.V. Krishnan, J.M. Vohs, R.J. Gorte, J. Electrochem. Soc. 151 (2004) A604–A608.